Probing the mechanism of the peroxiredoxin decamer interaction with its reductase sulfiredoxin from the single molecule to the solution scale

Audrey Beaussart, Florent Canonico, Hortense Mazon, Jorge Hidalgo, Sarah Cianférani, Hélène Le Cordier, Alexandre Kriznik, Sophie Rahuel-Clermont

To cite this version:

Audrey Beaussart, Florent Canonico, Hortense Mazon, Jorge Hidalgo, Sarah Cianférani, et al.. Probing the mechanism of the peroxiredoxin decamer interaction with its reductase sulfiredoxin from the single molecule to the solution scale. Nanoscale Horizons, 2022, 7 (5), pp.515-525. 10.1039/d2nh00037g . hal-03595966

HAL Id: hal-03595966
https://hal.univ-lorraine.fr/hal-03595966v1

Submitted on 7 Oct 2022

COMMUNICATION

Received 00th January 20xx,
Accepted 00th January 20xx

DOI: 10.1039/x0xx00000x

Probing the mechanism of peroxiredoxin decamer interaction with its reductase sulfiredoxin from the single molecule to the solution scale

Audrey Beaussart[a]†*, Florent Canonico[b]†, Hortense Mazon[b], Jorge Hidalgo[b], Sarah Cianférani[de], Hélène Le Cordier[b#], Alexandre Kriznik[bc] and Sophie Rahuel-Clermont[bc]*

Peroxiredoxins from the Prx1 subfamily (Prx) are highly regulated multifunctional proteins involved in oxidative stress response, redox signaling and cell protection. Prx is a homodimer that associates into a decamer. The monomer C-terminus plays intricate roles in Prx catalytic functions, decamer stability and interaction with its redox partner the small reductase Sulfiredoxin (Srx), that regulates the switch between Prx cellular functions. As only static structures of covalent Prx-Srx complexes have been reported, whether Srx binding dissociates the decameric assembly and how Prx subunit flexibility impacts complex formation is unknown. Here, we assessed the non-covalent interactions mechanism and dynamics in solution of *Saccharomyces cerevisiae* Srx with the Prx Tsa1 ten subunits at the decamer level *via* a combination of multiscale biophysical approaches including native mass spectrometry. We show that the ten subunits of the decamer can be saturated by ten Srx molecules and that the Tsa1 decamer in complex with Srx does not dissociate in solution. Furthermore, the binding events of atomic force microscopy (AFM) tip-grafted Srx molecules to Tsa1 individual subunits were relevant to interactions between free molecules in solution. Combined with protein engineering and rapid kinetics, the observation of peculiar AFM force-distance signatures revealed that Tsa1 C-terminus flexibility controls Tsa1/Srx two-step binding and dynamics and determines force-induced dissociation of Srx from each subunit of the decameric complex in a sequential or concerted mode. This combined approach from the solution to the single-molecule levels offers promising prospects for understanding oligomeric protein interaction with their partners.

Protein supramolecular assembly conveys means of regulation through multivalent interaction with partners, but designing experimental approaches for identifying these links is challenging. Peroxiredoxins are ubiquitous peroxide-reducing Cys enzymes, whose thiol redox reactivity, oligomeric structure and functions are intimately intertwined,[1] that act as major players in oxidative stress defense and in cell redox signaling networks.[2–4] Peroxiredoxins from the Prx1 subfamily (hereafter referred to as Prxs) exist as homooligomers. The Prx active unit is a symmetrical head-to-tail dimer stabilized by interactions between two β-strands that define the B-interface (Fig. 1A). They act as essential peroxide-reducing enzymes operating with a catalytic cysteine (Cys C_P), which reduces peroxide substrates with exquisite efficiency, leading to a sulfenic acid intermediate. Condensation with a resolving cysteine (Cys C_R) located in the C-terminal tail of the symmetric monomer produces a disulfide, which is reduced by thioredoxin or other cellular reductant system (Fig. S1). Importantly, Prx dimers associate into toroid structures as decamers, defining a dimer-dimer interface named A (Fig. 1A). The stability of Interface A is favored by the conformation of the C-terminal region in a fully folded FF state, and disfavored in the locally unfolded LU conformation adopted in the disulfide state (Fig. 1, Fig. S1).[5]

Eukaryotic Prxs are sensitive to post-translational modification of the catalytic Cys C_P to a sulfinic acid (also known as hyperoxidation), that occurs by reaction of a second peroxide molecule with the sulfenic acid intermediate and is critically regulated by competition with the FF/LU conformational transition along the Prx catalytic cycle (Fig. S1).[6–8] Prx C_P sulfinylation inactivates the peroxidase activity, allowing local buildup of H_2O_2 levels,[9] control of the redox state of reducing partners[10] and regulation of noncovalent interactions with signaling partners.[11] It also activates Prx chaperone function,[12,13] by stabilizing the FF conformation and Prx decamer state[14]. Sulfinylated Prx is reduced by the ATP-dependent sulfinic acid reductase Sulfiredoxin (Srx). By regulating the Prx sulfinylation level, Srx is associated with aging [12] and diseases like cancer.[15–17]

---

[a] *Université de Lorraine, CNRS, LIEC, F-54000 Nancy, France.*
[b] *Université de Lorraine, CNRS, IMoPA, F-54000 Nancy, France.*
[c] *Université de Lorraine, CNRS, INSERM, UMS2008 IBSLor, Biophysics and Structural Biology core facility, F-54000 Nancy, France.*
[d] *Laboratoire de Spectrométrie de Masse BioOrganique, Université de Strasbourg, CNRS, IPHC UMR 7178, 67000 Strasbourg, France.*
[e] *Infrastructure Nationale de Protéomique ProFI – FR2048 CNRS CEA, 67087 Strasbourg, France.*

[#] *Present address H.L.C.: LIEC, UMR 7360 CNRS-Université de Lorraine, Faculté des Sciences et Technologies, Bd des Aiguillettes, 54500 Vandœuvre-lès-Nancy, France.*

† *A.B. and F.C. contributed equally to this paper.*

Electronic Supplementary Information (ESI) available: [details of any supplementary information available should be included here]. See DOI: 10.1039/x0xx00000x

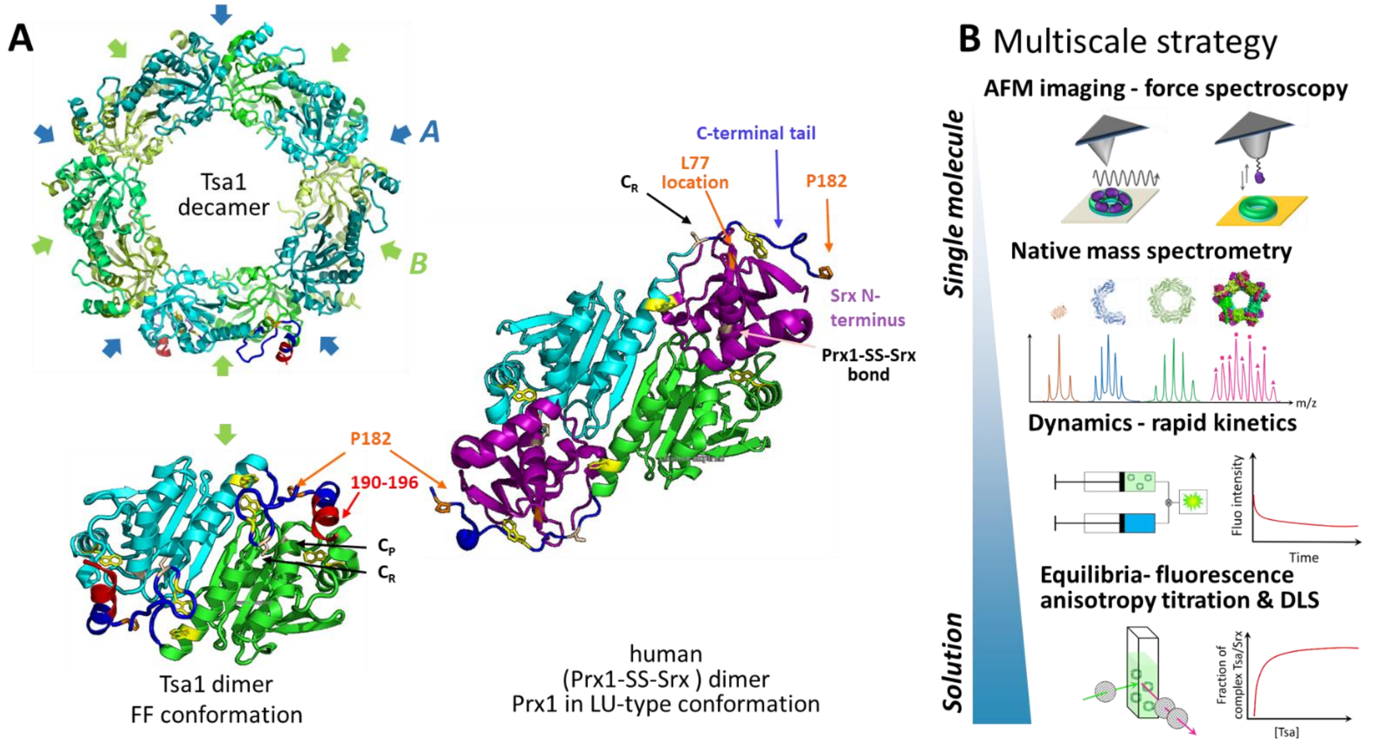

Figure 1. Assessing Prx/Srx interactions at multiscale levels. (A) Top, cartoon scheme of the reduced Tsa1$_{SH}$ X-ray structure from a top view (pdb code 3sbc); the A and B interfaces are indicated. Bottom, cartoon scheme of an isolated dimer of the Tsa1 decamer shown above, with subunits in green and cyan. The dimer is rotated 90° compared to the top view. The catalytic and resolving Cys C_P and C_R are indicated in light pink, the C-terminal tails in dark blue, Trp residues are in yellow and the location of the mutated residues is orange/red. Right, cartoon scheme of the X-ray structure of human dimeric Prx1-SS-Srx complex (pdb code 2rii), stabilized by a disulfide bond between Prx C_P and Srx catalytic Cys. The human Prx1 subunits are colored green and cyan as Tsa1$_{SH}$ and the C-terminal tail and P182 residues in the same color code. Human Srx is in purple, the human Prx1-SS-Srx disulfide bond and Prx1 Cys C_R in light pink. The human Srx residue corresponding to *S. cerevisiae* L77 on the backside interface is shown in orange. Location of Tsa1 Trp residues is shown in yellow. The Prx residues beyond P182 and Srx residues preceding A40 (labelled Srx N-terminus) are not defined in this structure. (B) Multiscale strategy developed in this study, based on approaches providing equilibrium and kinetic informations in solution to approaches allowing analyses at the level of single subunits within decamers (native mass spectrometry) or at the level of single decamers (AFM).

The crystal structure of human Prx1 dimer in complex with Srx revealed a double interface: the active site interface that enables to bring Prx sulfinylated C_P in proximity to Srx catalytic Cys; the backside interface consists of the Prx C-terminal tail unfolded around Srx, in a conformation akin to the LU state (Fig. 1A, Figs. S1, S2).[18] A similar structure was reported recently at the level of the decamer in the crystal state.[19] The Prx/Srx complex formation thus implies unfolding of the C-terminal Prx region that also could destabilize the decamer A interface, thus raising the questions whether Srx binding dissociates the decameric assembly and how Prx subunit C-terminus flexibility impacts complex formation. However, presently the mechanism and dynamics in solution of Prx decamer interaction with its partner proteins like Srx are unknown. Their exploration requires to monitor non-covalent dynamic complexes at the level of the decamer, by the use of techniques that allow measurements at the oligomer scale, such as single-molecule and native mass spectrometry techniques.

Atomic force microscopy (AFM) has been instrumental in imaging proteins oligomeric state and supramolecular assembly at high resolution.[20–24] In complement to electronic and X-ray crystallography, the technique allows the visualization of protein ultrastructures deposited on a substrate in liquid and in 3-dimensions, in real-time with minimal sample preparation. AFM also permits to quantify the forces involved in molecular interactions by decorating the tip with specific biomolecules and recording force-distance curves while the tip is moved up and down towards the substrate in the so-called single-molecule force spectroscopy (SMFS) mode at the level of individual subunits of multimeric complex.[25–28]

We address here the mechanism of Srx interactions with the Prx decamer in solution and at multiple scale levels by combining AFM in imaging and force spectroscopy modes, native mass spectrometry, and bulk measurements *via* fluorescence anisotropy titration, dynamic light scattering and binding dynamics using rapid kinetics (Fig. 1B). We obtained the first images in liquid of decameric Tsa1, the major Prx in the yeast *Saccharomyces cerevisiae,* deposited on a substrate bound with ten Srx molecules. We show that binding of Srx does not induce dissociation of the decamer. Furthermore, SMFS using a tip grafted with multiple Srx molecules allowed to observe binding events with the Prx decamer that are relevant to interactions between free molecules in solution. Combined with protein engineering and rapid kinetics, the observation of peculiar force-distance signatures revealed that Prx C-terminal tail plays a critical role in the rupture dynamics of the decameric Prx/Srx complex. Altogether our results highlight the wider potential of this multiscale methodology to obtain highly pertinent correlations from structure to single

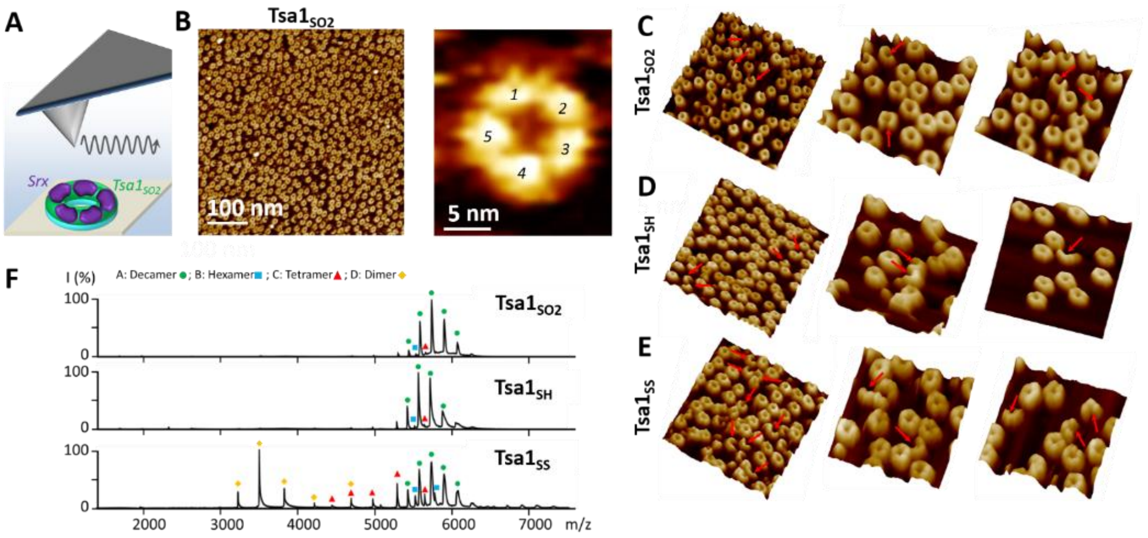

Figure 2. Evaluation of Tsa1 redox forms oligomeric state in solution. (A) Hyperoxidized Tsa1$_{SO2}$ decamer or Tsa1-SS-Srx decameric complex are deposited on a flat mica surface to image their molecular assembly at high resolution using peak force tapping AFM imaging in liquid conditions. (B) AFM image showing that Tsa1$_{SO2}$ adsorbed on the mica surface forms an almost complete monolayer of donut-shaped decamers. High resolution imaging of Tsa1$_{SO2}$ clearly reveals the 5 dimers composing the decamer. (C-E) Tsa1$_{SO2}$ (C), Tsa1$_{SH}$ (D) and Tsa1$_{SS}$ (E) structures are mostly donut-shaped assemblies, containing a significant fraction of uncomplete rings composed of octamers or hexamers, as highlighted by the red arrows. (F) Electrospray ionization mass spectra in native conditions of Tsa1 redox forms showing the dissociation of the decamer (experimental/theoretical mass for each form) (●; 215,031 ± 47 Da/214,905 Da for Tsa1$_{SO2}$, 214,592 ± 9 Da/214,585 Da for Tsa1$_{SH}$ and 214,791 ± 142 Da/214,575 Da for Tsa1$_{SS}$) into hexamers (■; 128,749 ± 18 Da/128,745 Da for Tsa1$_{SS}$), tetramers (▲; 85,840 ± 23 Da/85,830 Da for Tsa1$_{SS}$) and dimers (◆; 42,915 ± 2 Da/42,915 Da for Tsa1$_{SS}$) in the gas phase at Vc= 80 V.

molecule and solution behavior and answer mechanistic questions on oligomeric proteins multivalent interactions.

RESULTS AND DISCUSSION

Assessing the oligomeric architecture of Tsa1 redox forms in solution. We first assessed the behavior of Tsa1 redox forms, *i. e.* the reduced Tsa1$_{SH}$, disulfide oxidized Tsa1$_{SS}$ and sulfinylated hyperoxidized Tsa1$_{SO2}$ (Fig. S1) by high resolution AFM imaging in buffer at physiological pH. Tsa1 solution was deposited on atomically flat freshly cleaved mica and the surface was then imaged in liquid conditions to avoid any artefacts that could be induced by a drying step, using peak force tapping AFM imaging (Fig. 2A). As seen on Fig. 2B, the hyperoxidized species Tsa1$_{SO2}$ forms a layer of donut-shaped decameric rings homogeneously oriented flat, almost entirely covering the mica surface, similar to previous observations.[29,30] Imaging these structures at higher resolution allows to precisely distinguish the 5 dimers constituting the decamers (Fig. 2B, 3C). Imaging the other Tsa1 redoxomers -the reduced Tsa1$_{SH}$ and the oxidized C$_P$-C$_R$ disulfide Tsa1$_{SS}$ forms- produced similar images (Fig. 2D-E), suggesting that even at the concentration as low as 100 nM, purified Tsa1 primarily exists in solution as a decamer, including in the disulfide state. However, crescent-shaped structures were also observed amongst decamers (red arrows on Fig. 2C-E) with a frequency of 2.8, 2.7 and 12.5 %, in Tsa1$_{SO2,}$ Tsa1$_{SH}$ and Tsa1$_{SS}$ images, respectively. This suggests that dissociation of the decamer into octamer or hexamer can occur in solution or as a result of tip scanning and that the decamer structure is destabilized in the disulfide form, compared to the other redox forms, which is consistent with previous observations on Prxs from various origins.[31–34] We then analyzed the Tsa1 redox forms by native mass spectrometry that provides a resolution allowing the observation of intermediate oligomers with 2 to 8 subunits for human Prx3.[35] Fig. 2F shows that at low acceleration voltage (Vc=80 V) conditions (with minimum perturbation of non-covalent interactions), the reduced and hyperoxidized Tsa1 are decamers, while the Tsa1$_{SS}$ partially dissociates into dimers and a small fraction of tetramers and hexamers, a tendency confirmed in slightly more energetic conditions (Vc = 120 V, Fig. S3). This supports that the crescent-shape images correspond to oligomers with intermediate stoichiometry (2 to 6 subunits), and that the AFM images provide a snapshot of the oligomeric states of Tsa1 in solution discarding the hypothesis that the dissociation is induced by AFM tip scanning. However, we cannot exclude that -as suggested by their oriented deposition- interaction of the decamers with the mica contributes to stabilization of the decamers, compensating the dissociation that might occur at such low concentrations (0.1 µM).[33]

The height of the Tsa1$_{SO2}$ decamers extracted from the AFM images (3.3 ± 0.5 nm, Fig. 3C,F,G green sections) were in correlation with those obtained from the dimensions of Tsa1 decamer X-ray structure (4.6 nm, Fig. 3E left), confirming the observation of a single layer of decamers. The subtle lower height value obtained from AFM measurements might correspond to a slight collapse of the structures when deposited on the mica or a little indentation of the AFM tip while scanning the decamers. Vertical profiles of the rings were characterized by two summits -or peaks- (Fig. 3F) allowing to measure horizontal peak-to-peak dimensions of 8.5 ± 0.5 nm, perfectly consistent with the value of 8.7 nm deduced from the crystal structure (Fig. 3E,F,G). No such direct comparison could be done on the total width of the domains, as the value from the AFM images can be distorted by the tip convolution. Indeed, the total width extracted from AFM images (equal to the sum of the peak-to-peak distance plus twice the width of the peak-to-base, *i.e.* 17.3 nm for Tsa1$_{SO2}$; Fig. 3F) is larger than the 12.8 nm of the X-ray structure (Fig. 3E, left). The overall dimensions of the reduced and disulfide forms of Tsa1 deposited on the surface were in the same range as Tsa1$_{SO2}$ (Fig. S4).

Altogether, the original combination of high-resolution AFM imaging and native mass spectrometry allows to sense heterogeneities between subunits within the toroidal structures, which prompted us to follow the same approach to probe the decamers in interaction with its partner Srx.

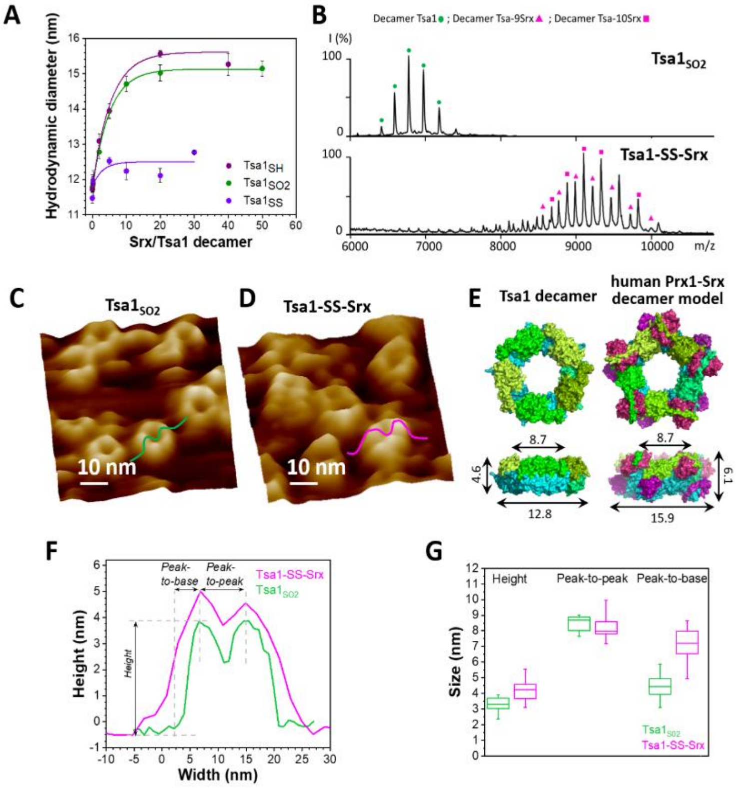

Figure 3. Srx binding increases the width and height of the Tsa1 ring structure. (A) Hydrodynamic diameter of Tsa1$_{SO2}$, Tsa1$_{SH}$ and Tsa1$_{SS}$ decamers measured by DLS as a function of the Srx:Tsa1 stoichiometry. Srx$^{C48S\ C84A\ C106V}$ mutant was used with Tsa1$_{SS}$ to avoid disulfide bond exchange. Data are representative of n=2 independent experiments using different proteins samples. (B) Electrospray ionization mass spectra in native conditions of the Tsa1$_{SO2}$ decamer (●; 236,587 ± 37 Da/236,218 Da) and decameric Tsa1-SS-Srx complexes at Tsa1:Srx stoichiometries of 9 (▲;359,819 ± 9 Da/358,920 Da) and 10 (■ ; 373,393 ± 11 Da/372,468 Da) in the gas phase at acceleration voltage Vc = 80 V (experimental/theoretical mass for each form). (C,D) High resolution AFM images of Tsa1$_{SO2}$ (C) and Tsa1-SS-Srx complex (D) with cross sections used to determine decamers dimensions. (E) left, top and side views of Tsa1$_{SH}$ (code pdb 3sbc); right, top and side views of human Prx1-SS-Srx decameric model in surface mode, constructed by superimposition of the X-ray structure of five Prx1-SS-Srx dimers (code pdb 2rii) (Fig. 1A) on the Tsa1$_{SH}$ structure. The height, width and peak-to-peak dimensions (defined in panel f) are indicated on the side views. Superimposition and measurements were done using Pymol 2.2.2[62]. (F) Typical cross-sections of Tsa1$_{SO2}$ decamer (green) and Tsa1-SS-Srx complex (pink) extracted from AFM images in c and d. (G) Decamers dimensions shown by box charts. The bottom and top of the boxes represent the 25th and 75th percentiles, the whiskers the 10th and 90th percentiles and the horizontal bands the median. Data stem from measurements on at least: 25 donuts for Tsa1$_{SO2}$ and 15 complexes for Tsa1-SS-Srx. Differences between Tsa1$_{SO2}$ and Tsa1-SS-Srx were compared using two-sample t-tests. The peak-to base difference was considered statistically significant ($p<0.05$).

The Tsa1 decamer in complex with Srx does not dissociate in solution. The Prx/Srx complex formation involves unfolding of the C-terminal Prx region that also participates in stabilizing the decamer A interface (Fig. 1A). Whether the binding of Srx to Prx destabilizes or induces the dissociation of the decamer is presently unknown in solution. We thus studied Tsa1 structures in interaction with Srx using similar experimental strategy as above. As a preliminary to the observation of the Tsa1/Srx complex, we first addressed the question whether the Tsa1 decamer could be non-covalently saturated by 10 Srx molecules, using dynamic light scattering (DLS) (Fig. 3A). Titration of Tsa1$_{SO2}$ by Srx resulted in an increase of the Tsa1 hydrodynamic diameter from 11.8 nm to a plateau of ~ 15.2 nm obtained for ratios above 10 Srx to one Tsa1 decamer, suggesting that Tsa1 can be saturated by 10 Srx molecules in solution. Similar result was obtained with Tsa1$_{SH}$. Analogous experiment using Tsa1$_{SS}$ in which the C-terminal tail is locked by a disulfide bond between Cys C$_P$ and C$_R$ with Srx$^{C48S\ C84A\ C106V}$ (used here to avoid any disulfide bond exchange) resulted in variation of the hydrodynamic diameter between 12 and 13 nm, indicating that Tsa1$_{SS}$ did not form specific non-covalent complexes, as expected.

To support that the Tsa1/Srx complex exists as a decamer, we performed native mass spectrometry on the Tsa1 decamer in complex with Srx molecules (Fig. 3B), stabilized by a disulfide bond between the catalytic Cys residues of each Srx and Tsa1 Cys C$_P$, which mimicks the catalytic thiolsulfinate intermediate of the Srx catalytic mechanism.[36,37] This strategy previously proved to be successful to resolve the X-ray structure of the human Prx1/Srx complex (Fig. 1).[18,19] The specificity and completeness of the reaction between Tsa1 C$_P$ and Srx was ensured by using mutants that only retain the catalytic Cys residues, C$_P$ in Tsa1 and C84 in Srx. Reacting Tsa1^{C171A} C$_P$ pre-activated by 2,2'-dipyridyldisulfide (2PDS) with Srx$^{C48A\ C106V}$ yielded the Tsa1^{C171A}-SS-Srx$^{C48A\ C106V}$ complex, referred to as Tsa1-SS-Srx, as checked by non-reducing SDS-PAGE (Fig. S5, Table S1). Native mass spectrometry analysis showed that the Tsa1-SS-Srx solution is a mixture of decameric Tsa1 complexes with 9 and 10 Srx bound (Fig. 3B), in accordance with the DLS titration (Fig. 3A).

Next, to observe the morphology of the Tsa1 decamer in interaction with Srx, we imaged by AFM a Tsa1-SS-Srx solution deposited on the mica-surface (Fig. 3D). Statistical analysis of the AFM-imaged decamers dimensions reveals that binding of Srx induces no significant changes on the peak-to-peak distances (8.2 ± 0.7 nm), but increases the height and peak-to-base dimensions of the rings by 0.9 nm (from 3.3 to 4.2 nm) and 2.7 nm, (from 4.4 to 7.1 nm) respectively (Fig. 3F,G). Although the tip convolution might increase the length of the peak-to-base in absolute value, the relative difference between these dimensions measured before and after addition of Srx remains significant (Fig. 3F,G). These values were then compared to the dimensions deduced from a model of the decameric complex constructed by superposition of five duplicates of the human disulfide $(Prx1\text{-}SS\text{-}Srx)_2$ complex[18] and the $Tsa1_{SH}$ decamer X-ray structures.[38] This model suggested an increase of 1.5 nm of the height and 1.6 nm of the peak-to-base dimensions upon Srx binding (Fig. 3E right), in good agreement with the tendency obtained by AFM (Fig. 3G). This supports that the mechanism of interaction between Srx and Tsa1 can be studied in solution at the level of the decamer.

C-terminus flexibility affects Tsa1/Srx two-step binding. The importance of Prx C-terminal tail in the backside interface with Srx shown previously[18] prompted us to investigate the role of this region in the dynamics of interaction of the Tsa1 decamer with Srx. We prepared the P182L and Δ190-196 Tsa1 mutants (Table S1), that exist as decamers (with hydrodynamic radii of 12.6 ± 0.5 and 13.7 ± 0.5 nm, respectively, similar to wild-type Tsa1). These mutants adopt primarily the LU conformation, as shown by their near-UV circular dichroism spectra similar to $Tsa1_{SS}$ which is locked in the LU conformation[7], suggesting increased C-terminus flexibility (Fig. S6). For this reason these mutants are not susceptible to hyperoxidation and were used in the reduced form.[7,39–41] The binding properties with Srx were thus compared in solution with reduced wild-type $Tsa1_{SH}$. Srx bound to both P182L and Δ190-196 $Tsa1_{SH}$ with increased affinity, as shown by K_D values of 5.9 ± 1.2 and 5.0 ± 1.7 µM, respectively, compared to 10.8 ± 3.0 µM measured for the wild-type by fluorescence anisotropy titration (Fig. 4A). To correlate these properties with the dynamics of interaction in solution, we measured the dissociation kinetics of the Tsa1/Srx complex by monitoring Tsa1 Trp intrinsic fluorescence upon rapid dilution of Tsa1/Srx mixtures in solution using a stopped flow apparatus. Srx has no Trp residues while Tsa1 contains 3 Trp, one located close to the active site (W83), another in helix α4 preceding the C-terminal tail (W161), and the last in the C-terminal tail (W173) that are likely to be sensitive to the changes in molecular environment induced by Srx binding (Fig. 1A, Fig. S2). Indeed, using this probe to monitor dilution-induced dissociation, we observed that wild-type $Tsa1_{SH}$ dissociates from Srx by following biphasic kinetics. The data set was analyzed globally according to a two-step model, consisting of a first order step reflecting a conformational

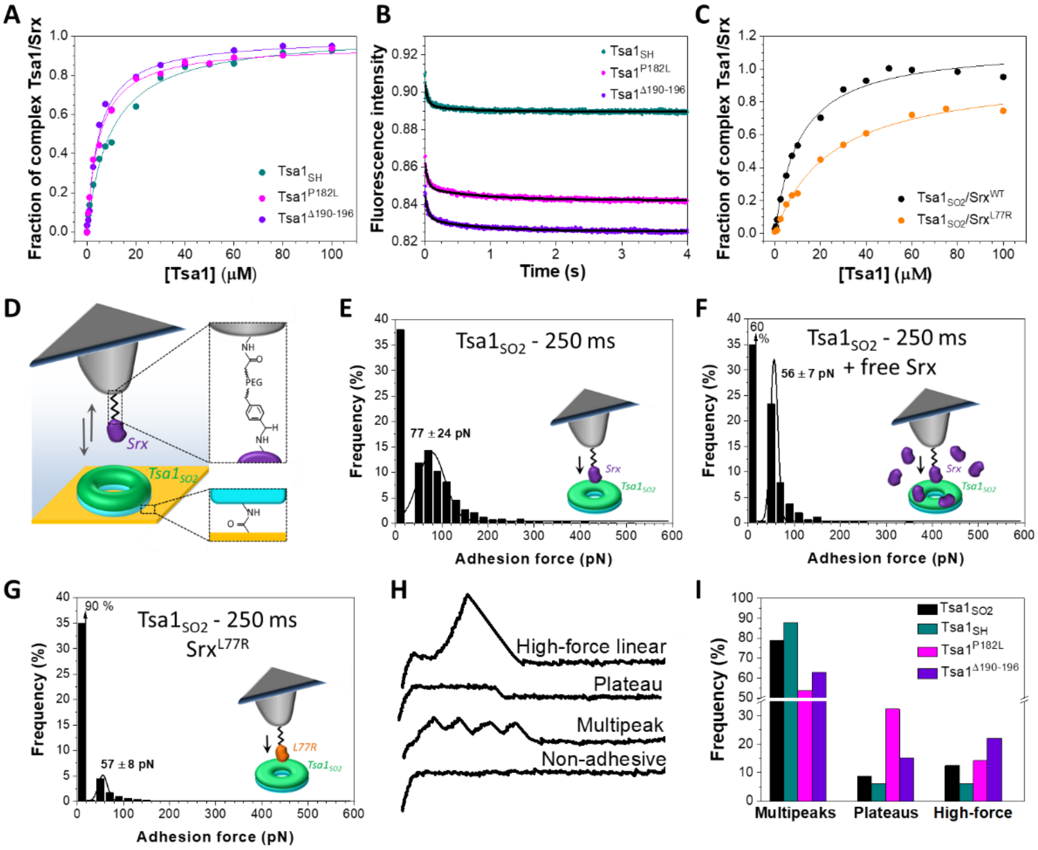

Figure. 4. Impact of Tsa1 C-terminal region flexibility on Srx interaction mechanism. (A,C) Fluorescence anisotropy titration of (A) AlexaFluor labelled Srx by wild-type, P182L and Δ190-196 mutants $Tsa1_{SH}$ and (C) wild-type Srx and SrxL77R N-terminally labelled with AlexaFluor by $Tsa1_{SO2}$.. Data representative of n = 2 or 3 independent experiments using different proteins batches are fitted using a single site model equation (solid line). (B) Representative dilution-induced dissociation kinetics of the non-covalent $Tsa1_{SH}$/Srx complexes in solution for wild-type, P182L and Δ190-196 Tsa1 monitored by Trp intrinsic fluorescence in a stopped flow apparatus. Tsa1 (subunits) and Srx concentrations are 2.5 and 20 µM, respectively. The curves are fitted as described in Suppl. information. Data are representative of n = 3 independent experiments using different proteins samples. (D) For AFM single-molecule force spectroscopy, Srx is covalently bound to the tip using an acetal-PEG linker. The tip is approached and retracted from Tsa1 covalently attached to a gold surface. (E) Adhesion force histograms of Srx binding to $Tsa1_{SO2}$ with 250 ms contact time. (F,G) Specificity of the Srx/$Tsa1_{SO2}$ interaction confirmed by a significant reduction of the adhesion frequency in presence of free competing Srx (F) or using L77R Srx mutant (G). Each histogram has been plotted from 3072 force curves obtained from 3 independent experiments with different functionalized tips. Black lines correspond to Gaussian fits and the values are the centre ± standard deviation. (H,I) Representative force-distance signatures (H) with their frequency (I) for wild type $Tsa1_{SH}$, $Tsa1_{SO2,}$ P182L and Δ190-196 mutants, obtained from 3072 force curves from 3 independent measurements for each form of Tsa1 and calculated relative to the total of assigned curves, excluding the non-adhesive and hybrid profiles.

event occurring within the complex, modelized by equilibrium between two conformers Tsa1•Srx and Tsa1•Srx* forms, and a second order step reflecting dissociation (Fig. S7 A,B). Using the same scheme to analyze the mirror association experiment performed in similar conditions by rapid mixing of Tsa1 et Srx solutions, gave satisfactory fits and overall consistent rate constants values (Fig. S7C, Table S2), confirming that Trp fluorescence probe is suitable for the study of Tsa1/Srx interactions. These results suggested that wild-type Tsa1$_{SH}$ dissociates from Srx with a k$_{-1}$ rate constant of 18.8 ± 2.8 s^{-1}, which was reduced to 11.8 ± 3.0 s^{-1} and 7.5 ± 2.2 s^{-1} for the P182L and Δ190-196 Tsa1 mutants respectively (Fig. 4B, Table S2). The same trends were obtained from the association experiment, supporting that a slower bimolecular dissociation kinetics likely afforded by more flexible C-terminal Tsa1 region contributes to the higher affinity of Srx for these mutants.

To understand how these binding features translate at the level of the decamer, we addressed Srx interactions on Tsa1 single decamers by AFM in force spectroscopy mode. Purified Tsa1 was bound to gold surface modified with COOH-terminated thiols using NHS-EDC chemistry whereas Srx was covalently attached on AFM tips with a ~6 nm long PEG-benzaldehyde linker (Fig. 4D). The grafting procedure to the tip was carried out under conditions which favor deprotonation of N-terminal amine (pH 8.5), thus leading to an oriented binding of the protein to the tip.[18,42] Adhesion was then assessed with the Srx substrate, the hyperoxidized Tsa1$_{SO2}$. Fig. 4E displays the adhesion force histograms extracted from 3072 force-distances curves each, obtained using 3 independent tips on different 1 x 1 µm^2 areas of the Tsa1$_{SO2}$ surfaces with a retraction speed of 1000 nm s^{-1}. Only the last adhesion peak, corresponding to the force at rupture, was considered for the force histogram (Fig. S8A). When Srx and Tsa1$_{SO2}$ are set to interact for 250 ms, a substantial proportion of the force curves (63 %, Fig. 4E) showed adhesive events between the two enzymes, with a mean adhesion force (which is displayed at the maximum of the Gaussian fit and corresponds to the force which is needed to break the interaction when Srx binds to Tsa1) of 60 ± 4 pN. Less frequent events at 95 ± 24 pN were also observed, that could reflect the simultaneous rupture of two Srx molecules on the tip from two Tsa1$_{SO2}$ subunits on the surface (Fig. 4E). Reducing the contact time between the two enzymes from 250 to 0 ms decreases the adhesion frequency from 63% (Fig. 4E) to 14% (Fig. S8B) without changing the mean adhesion forces, at around 55 ± 8 pN.

At 250 ms contact time, a major reduction of the adhesion frequency was observed upon addition of free Srx in the AFM liquid set-up although the general shape of the histogram, presenting two maxima, was not drastically modified (Fig. 4F). This suggested that a competition occurs between free and grafted Srx for binding to a decamer and that the measured adhesion events on Fig. 4E correspond to interactions between Srx on the tip with the Tsa1$_{SO2}$ proteins bound to the surface. To substantiate this result, we used the Srx^{L77R} mutant designed to impact the Srx backside interface with Tsa1 (Fig. 1A). Mutation of the corresponding residue in human Srx (Y92R) (Fig. S2) was shown to severely alter the interaction with human hyperoxidized Prx1[18]. Indeed, the dissociation constant of *S. cerevisiae* Srx^{L77R} for Tsa1$_{SO2}$ measured by fluorescence anisotropy titration increased from 12.6 ± 2.5 to 27.1 ± 1.3 µM (Fig. 4C). The AFM adhesion frequency for Tsa1$_{SO2}$ at 250 ms contact time was reduced from 63 % (Fig. 4E) to 10 % for the L77R variant (Fig. 4G), whereas the maximum adhesion force was not affected. Furthermore, the adhesion frequencies of Srx-coated AFM tips to surfaces decorated with P182L and Δ190-196 Tsa1$_{SH}$ mutants were significantly higher as compared to wild-type Tsa1$_{SH}$ (Fig. S9). This suggests that alteration of the native Tsa1/Srx interaction on the backside interface is connected to the binding propensity, which translated into the adhesion probability as measured by AFM force spectroscopy. A very low adhesion frequency of 14% was observed in similar conditions for Tsa1$_{SS}$ (Fig. S10A), in accordance with the DLS titration (Fig. 3A). Given the good correlation between the anisotropy titration and AFM results, we propose that the adhesion events measured by force spectroscopy on Fig. 4E reflect Srx/Tsa1$_{SO2}$ interactions relevant to those occurring between the free proteins in solution.

To get insight into the interaction mechanisms, we further analyzed the multiple force-distance curves recorded between Srx and Tsa1$_{SO2}$. Distinct remarkable signatures were identified and classified in 5 forces curves families: the non-adhesive curves, the multipeaks, the force plateaus, the high linear forces (see representative force curves in Fig. 4H), and a last category of forces including undefined or hybrids of the profiles described above (Fig. S8C). The proportion of the 3 well-defined profiles (*i.e.* the multipeaks, the force plateaus and the high linear forces) vary for the Tsa1 redox and mutant forms (Fig. 4I). The origin of these events is discussed below.

Peculiar signatures reveal two modes of force-induced Srx dissociation from the Tsa1 decamer. A first category of signatures consists in force profiles containing well-defined multipeaks, most frequently 1 to 4 peaks, and rare events with 5 peaks, of almost constant adhesion force (< 100 pN; Fig. 5A) and spaced by 15.7 ± 6.7 nm (Fig. S8D). The linking chemistry used here to covalently attach Srx to the tip[43] and the nominal value of the tip apex radius of 10 nm up to 40 nm radius (as given by the provider Bruker), although statistically resulting in the grafting of one single molecule at the apex of the tip,[43,44] can lead to attachment of up to 13 Srx molecules on the tip (considering a half sphere geometry).[43] Thus, we suggest that these events reflect the interaction of several Srx molecules decorating the tip with the upper ring of the decameric structure, in accordance with AFM imaging that showed that decamers lie flat on the mica surface (Fig. 2B). Upon the approach phase, the AFM tip might indent within the ring-shaped decamer structure whose dimensions are in the range of the tip diameter, also enabling other Srx molecules grafted on the side of the tip to interact with accessible Tsa1 subunits (Fig. 5B, case 1), yet we cannot exclude interaction with neighboring decamer on the surface (Fig. 5B, case 2). Observation of reproducible multipeak patterns upon hundreds of force measurements on the adhesion maps (1024 force-distances curves recorded with each functionalized tips) suggests that the native folding of the tip-grafted Srx molecule is preserved and that the protein either does not unfold or unfolds and refolds on repeated association/dissociation events. Additionally, the force-distance signatures could not be adequately fitted using classical protein unfolding models (*e.g* Worm-like-chain model[45]), supporting that the force-induced Tsa1/Srx binding and dissociation does not result in the unfolding of both enzymes upon pulling. Thus, owing to the N-terminal oriented Srx grafting on the tip, the observed force-induced dissociation could proceed *via* traction of the Tsa1 C-terminal tail by Srx bound at the backside interface (Fig. 5C) (> 16 residues-length for Tsa1, ~6 nm, Fig. S2), that adds to extension of the Srx N-terminal segment preceding those involved in the backside interface (~10 residues, 4 nm, , Fig. S2) and the 6 nm-linker, consistent with the ~16 nm spacing between rupture events.

The increasing rupture distances would then reflect successive dissociation of Srx molecules from the Prx C-terminus subunits (Fig. 5C). Indeed, the relatively high standard deviation (15.7 ± 6.7 nm) (Fig. S8D) of the interpeak distance is consistent with Srx grafted at different heights on the tip and with the intrinsic rugosity of gold surfaces used for force spectroscopy measurements that may then slightly tilt the orientation of the decamers. Accordingly, increasing the contact time from 0 to 250 ms enhances the frequency of signatures with more than 1 peak (Fig. 5A), suggesting increased probability to form more than one interaction with the accessible Tsa1 subunits of a single decamer before being broken upon tip retraction. To further support this interpretation, we studied the interaction between Srx and a dimeric Tsa1^{S79E} mutant whose A interface is destabilized by introduction of two facing Glu residues,[18,38] confirmed by its DLS hydrodynamic diameter of 6.3 nm (*vs.* 11.8 nm for the Tsa1$_{SO2}$ decamer), and by native mass spectrometry (Fig. S10C). This mutant showed lower adhesion of 31% compared to Tsa1$_{SO2}$ (Fig. S10B) allowing analysis of the multiple force-distance curves profiles, which revealed mostly one- and two-peaks signatures (Fig. 5A). This behavior is consistent with one or two Srx grafted on the tip interacting with a dimer. Very rare three- and four-peaks events were observed, possibly explained by interaction with neighboring dimers.

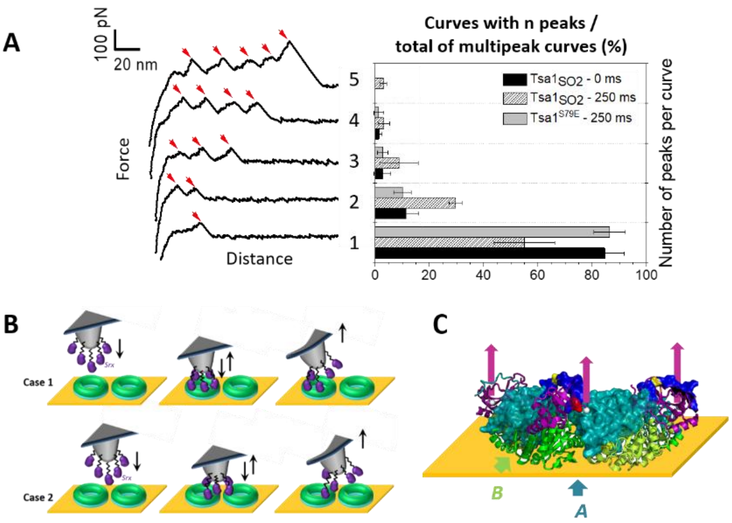

Figure. 5. Srx interaction with Tsa1 decamer reveals multipeak force-distance signatures. (A) Representative force-distances curves (left) obtained when recording force spectroscopy measurements between Srx and Tsa1$_{SO2}$, revealing well-defined multipeaks ranging from 1 to 5 peaks. Corresponding frequencies (right) of the multipeaks categories over the total number of multipeaks for Tsa1$_{SO2}$ at 0 and 250 ms contact time, and for the dimeric Tsa1^{S79E} mutant at 250 ms contact time, obtained from 3072 force measurements for each contact time, from 3 independent experiments with different functionalized tips. Error bars correspond to the standard deviations between tips. (B) Proposed schematics of the interaction mechanism generating the multipeaks signatures, where five Srx bound to the AFM tip interact with the upper ring of one (case 1) or two (case 2) Tsa1 ring-shaped structure(s) lying on the gold surface. (C) Illustration in cartoon mode of a composite decamer, in which the upper ring corresponds to human Prx1-SS-Srx subunits from the model shown in Fig. 3E, and the lower ring corresponds to Tsa1$_{SH}$ subunits covalently bound to the surface. The human Prx1 subunit are shown in surface mode. The colour code is the same as in Fig. 1A. Only the 3 dimers on the front are shown for clarity. The location of the last residue of Srx N-terminus defined in the crystal structure is shown as a white ball and the arrows represent the traction of the AFM tip imposed by Srx grafted to the tip on the Prx C-terminal tail.

A second category of force-distance profiles was observed, consisting in well-defined plateaus occurring at near constant force of ~50 pN along distances ranging from 20 to 100 nm with a majority of curves extending at 40 nm (Fig. 6A,B*)*. Strikingly*,* whereas the frequency of plateaus was low and almost similar for Tsa1$_{SO2}$ and Tsa$_{SH}$ (6.2 and 8.7 %, respectively), they reached up to 15 and 32 % for the Δ190-196 and P182L Tsa1 mutants, respectively, whose C-terminus flexibility is enhanced (Fig. 4I). If those peculiar signatures would reflect some unspecific interactions of no biological origin (such as artifactual hydrophobic or electrostatic interactions), one would expect that they would be encountered with the same frequency for all Tsa1 forms. However, because the plateau signatures were correlated with

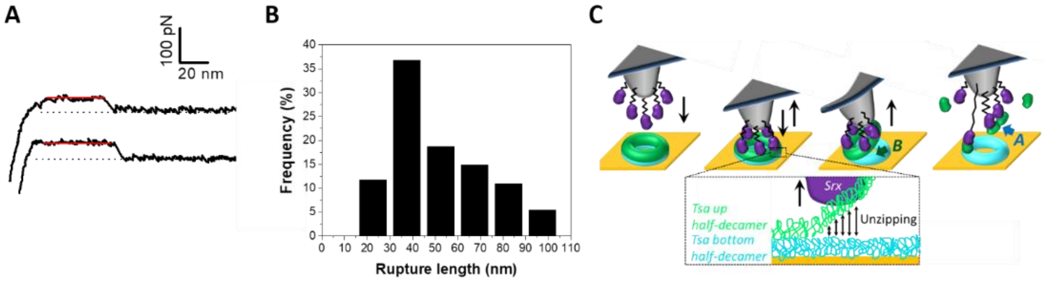

Figure. 6. Srx interaction with Tsa1 decamer shows constant force plateaus force-distance signatures. (A) Representative force-distance curves of the linear plateaus. (B) Histogram of the frequency of the plateau length, measured from 128 force curves for wild-type Tsa1$_{SO2}$. (C) Schematics of the suggested mechanism, where synergic traction of multiple Srx bound to the upper half-decamer of the donut would induce unzipping from the bottom half-decamer covalently bound to the gold surface.

binding properties to Srx in solution, we speculate that the enhanced adhesion between Srx and the upper half-decamer (formed by the 5 Tsa1 monomers at the interface with the buffer solution; Fig 6C, green subunits) could promote the concerted detachment from the 5 monomers covalently grafted on the gold surface (Fig 6C, cyan subunits). However, the affinity of Srx with individual Tsa1 subunits is moderate (K_D in the 10 µM range), and the β-strand interaction forming the B interface likely is tight. Thus, the synergic traction of several Srx on the C-terminal tails of Tsa1 subunits of one decamer, favored by mutations providing stronger interaction, would make possible the disruption of the B (and consequently the A interfaces) by the rupture of the β-strands H-bonds upon constant force following an unzipping mechanism, an interpretation supported by the following arguments. Such plateaus are evocative of the signatures measured for the mechanical unzipping in other systems such as β-sheet interactions in pathological and functional amyloids.[46,47] Although amyloid bonds are responsible for the very strong attachment of *e.g.* yeast to the epithelial layer, pulling on amyloid proteins with an AFM tip perpendicularly to the fiber axis was reported to allow mechanical unzipping of β-sheets at constant low force around 35 pN,[47] similar to the average strength of the plateaus observed here around 50 pN (Fig. 6A). Because the force required to rupture β-sheets should be strongly dependent on the pulling direction,[48] depending on the positioning of the AFM tip relative to the Tsa1 decamer, the upper-half decamer could be lifted up at a constant low force as -schematically- would be a yogurt peelable lid. Accordingly, the measured average length of the plateaus is consistent with an unzipping mechanism occurring along the perimeter of a decamer of 6.4 nm radius (perimeter = 2π x 6.4 nm = 40.2 nm; Fig. 6C). In conclusion, the observation of such force-induced plateaus further highlights the critical role of the C-terminal tail in the interaction of Srx with the Tsa1 decamer.

Disulfide bond formation between Srx and Tsa1$_{SO2}$ revealed by AFM force spectroscopy. Interestingly, another distinct, infrequent and peculiar force-distance profile was observed in force-distance experiments, corresponding to high force linear (HF) peaks ranging from 100 pN to > 1 nN (Fig. 4I, 7A,B). With Tsa1$_{SO2}$, force distribution showed a maximum at 450 pN extending up to 1100 pN (Fig. 7B). Increasing the contact time between the tip and the surface from 250 ms to 1 s expanded the distribution to higher forces, with a significant number of occurrences above 1 nN, up to 1.3 nN (Fig. 7B). Tsa1 and Srx are Cys-containing redox sensitive proteins prone to unspecific oxidation by reactive oxygen species. We thus hypothesized that the Srx Cys residues involved in catalysis (C84 and C48)[49] could oxidize to sulfenic acid or disulfide due to reactive oxygen species present in the solution, and react with Tsa1$_{SO2}$ residual Cys (C_R) to form an intermolecular disulfide, a process favored by a longer contact delay to allow conformational orientation suitable for the Cys residues to react. Accordingly, the P182L and Δ190-196 Tsa1 mutants whose C-terminal region likely is more flexible, show increased high force signature frequency (Fig 4I).

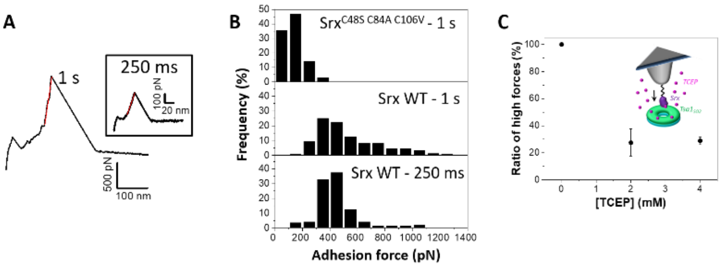

Figure. 7. Srx interaction with Tsa1 decamer reveals high linear force (HF) signature consistent with disulfide bond formation. (A) Representative high linear forces obtained when Srx is interacting with Tsa1SO2 for a contact time set to 1 s and 250 ms (a, inset). (B) Histograms of the adhesion force frequency of high linear forces for 250 ms (wild-type Srx) and 1 s contact time (SrxC48S C84A C106V and wild-type Srx). Histograms have been built from 168 HF curves for 250 ms and 160 HF curves for 1s contact time. (C) Impact of the addition of the disulfide bond reducer TCEP in the AFM liquid cell on the frequency of appearance of HF signatures. Each point in c corresponds to the number of HF over 2048 force curves obtained from 2 independent experiments with different functionalized tips.

We showed that, for 1 s surface delay experiments, increasing TCEP (tris(2-carboxyethyl)phosphine) -a reducing agent breaking disulfide bonds- from 0 to 4 mM decreases the number of HF peaks by 70 % (Fig. 7C), thus supporting HF peaks corresponding to disulfide bond rupture. Based on the literature [50,51] the formation and breaking of covalent bonds between both proteins would be reflected in the highest values of forces (above 1 nN). Although the origin of the linear forces ranging from 400 to 1000 pN cannot be precisely determined, we believe that they are associated with the interactions between the Cys of both Srx and Tsa1, as demonstrated by performing a similar experiment using the Srx$^{C48S\ C84A\ C106V}$ mutant in which all Cys are substituted. The global adhesion frequency was similar to the wild-type Srx but it did not show any HF peaks above 400 pN, even at 1 s of contact time (Fig. 7B). However, these controls do not allow to discard that the 400-1000 pN forces could also be due to the Srx-cysteine binding to the gold surface as this would result in the same range of forces.[52]

This observation opens significant opportunity to expand the use of single-molecule force-based techniques in thiol redox enzymology. AFM-based approaches have been used so far mostly to study the rupture of disulfide bonds by disulfide exchange reactions catalyzed by thioredoxin or related enzymes.[53–55] Our results thus open the possibility to study the formation of covalent bonds involved in enzyme-catalyzed reaction by AFM-based techniques.

Conclusions

How decameric Prxs interact with their partner proteins is essential to understand the regulation of their multiple functions. Indeed, *in vivo* full hyperoxidation of the Prx decamers has been shown,[56,57] which implies that multiple subunits are substrate of Srx. Given the high concentration of cytosolic Prx from the Prx1 family (~20 µM for Tsa1[58]), and relatively lower concentration of Srx (~75 folds less than Tsa1[58]), interaction of multiple Srx on a single decamer could provide a biological advantage to regenerate a decamer to the fully reduced form *vs.* heterogeneous complexes of reduced and hyperoxidized subunits, which would have *e.g.* lower peroxidase activity. This could be favored by Srx binding cooperatively to the decamer. Although this idea is speculative, the present study gives insight into the formation of these complexes at the single decamer level, which is necessary to further address such questions.

Tsa1 decamer interaction with Srx have been resolved in solution at the decameric level by AFM imaging of a Tsa1(Srx)$_{10}$ complex stabilized covalently, using native mass spectrometry and DLS, showing that interaction of Srx does not induce dissociation of the decamer. Force spectroscopy assessment of the interaction between surface-bound Tsa1 decamer and tip-grafted with multiple Srx appeared to be relevant to the interaction between free molecules in solution and allowed to resolve the interaction of up to five Srx with Tsa1 subunits. Combining with investigation of the dynamics of Tsa1/Srx interactions using rapid kinetics revealed a two-step binding mechanism and showed the critical role of the Prx C-terminal tail in the binding mechanism, in accordance with sequential or concerted dissociation of tip-grafted Srx from the decamer shown by AFM peculiar force-distance signatures.

Overall, these highly pertinent correlations between affinity, kinetics, and single molecule data strongly support this multiscale methodology as a proficient method to further understand how protein supramolecular assembly regulates multivalent interaction with partners, such as binding mechanisms between Srx interaction and newly discovered substrates.[59] Finally, the formation of disulfide bond could also be observed from specific rupture signatures, which should open avenues for the study of the mechanisms allowing Prxs to act as redox relay,[60] and developing AFM as an new platform in thiol redox enzymology.

Author Contributions

The manuscript was written through contributions of all authors. All authors have given approval to the final version of the manuscript. AB, HM, SC and SRC designed research; AB, FC, HM, JH, HLC, and AK performed research; AB, FC, HM and SRC analyzed data; and AB and SRC wrote the paper.

Acknowledgements

We gratefully acknowledge J. Charbonnel for efficient technical help. This work was supported by ANR grant ANR-17-CE11-0034-02 to SRC, Ligue contre le Cancer to SRC, ANR grant ANR-20-CE34-0005-01 to AB, the Université de Lorraine, Université de Strasbourg and CNRS. The authors acknowledge support of the group by the "Impact Biomolecules" project of the "Lorraine Université d'Excellence" (Investissements d'avenir-ANR). This work was granted access to the Biophysics and structural biology core facility of UMS2008 IBSLor CNRS-UL-INSERM and the French Proteomic Infrastructure ProFI (ANR-10-INBS-08-03 grant).

Conflicts of interest

There are no conflicts to declare.

Notes and references

1 A. Perkins, K. J. Nelson, D. Parsonage, L. B. Poole and P. A. Karplus, *Trends in Biochemical Sciences*, 2015, **40**, 435–445.
2 S. Fourquet, M. E. Huang, B. D'Autreaux and M. B. Toledano, *Antioxid Redox Signal*, 2008, **10**, 1565–76.
3 S. G. Rhee, H. A. Woo and D. Kang, *Antioxidants & Redox Signaling*, 2017, **28**, 537–557.
4 D. E. Fomenko, A. Koc, N. Agisheva, M. Jacobsen, A. Kaya, M. Malinouski, J. C. Rutherford, K.-L. Siu, D.-Y. Jin, D. R. Winge and V. N. Gladyshev, *PNAS*, 2011, **108**, 2729–2734.
5 Z. A. Wood, L. B. Poole, R. R. Hantgan and P. A. Karplus, *Biochemistry*, 2002, **41**, 5493–5504.
6 Z. A. Wood, L. B. Poole and P. A. Karplus, *Science*, 2003, **300**, 650–653.
7 A. Kriznik, M. Libiad, H. Le Cordier, S. Boukhenouna, M. B. Toledano and S. Rahuel-Clermont, *ACS Catalysis*, 2020, 3326–3339.
8 A. Perkins, K. J. Nelson, J. R. Williams, D. Parsonage, L. B. Poole and P. A. Karplus, *Biochemistry*, 2013, **52**, 8708–8721.
9 I. S. Kil, S. K. Lee, K. W. Ryu, H. A. Woo, M.-C. Hu, S. H. Bae and S. G. Rhee, *Molecular Cell*, 2012, **46**, 584–594.
10 A. M. Day, J. D. Brown, S. R. Taylor, J. D. Rand, B. A. Morgan and E. A. Veal, *Molecular Cell*, 2012, **45**, 398–408.
11 B. Turner-Ivey, Y. Manevich, J. Schulte, E. Kistner-Griffin, A. Jezierska-Drutel, Y. Liu and C. A. Neumann, *Oncogene*, 2013, **32**, 5302–5314.
12 S. Hanzén, K. Vielfort, J. Yang, F. Roger, V. Andersson, S. Zamarbide-Forés, R. Andersson, L. Malm, G. Palais, B. Biteau, B. Liu, M. B. Toledano, M. Molin and T. Nyström, *Cell*, 2016, **166**, 140–151.
13 H. H. Jang, K. O. Lee, Y. H. Chi, B. G. Jung, S. K. Park, J. H. Park, J. R. Lee, S. S. Lee, J. C. Moon, J. W. Yun, Y. O. Choi, W. Y. Kim, J. S. Kang, G. W. Cheong, D. J. Yun, S. G. Rhee, M. J. Cho and S. Y. Lee, *Cell*, 2004, **117**, 625–35.
14 F. Teixeira, E. Tse, H. Castro, K. A. T. Makepeace, B. A. Meinen, C. H. Borchers, L. B. Poole, J. C. Bardwell, A. M. Tomás, D. R. Southworth and U. Jakob, *Nat Commun*, 2019, **10**, 659.
15 H. Jiang, L. Wu, J. Chen, M. Mishra, H. A. Chawsheen, H. Zhu and Q. Wei, *Mol Cancer Res*, 2015, **13**, 1554–1566.
16 Q. Wei, H. Jiang, Z. Xiao, A. Baker, M. R. Young, T. D. Veenstra and N. H. Colburn, *Proc Natl Acad Sci U S A*, 2011, **108**, 7004–9.
17 H. Kim, G.-R. Lee, J. Kim, J. Y. Baek, Y.-J. Jo, S.-E. Hong, S. H. Kim, J. Lee, H. I. Lee, S.-K. Park, H. M. Kim, H. J. Lee, T.-S. Chang, S. G. Rhee, J.-S. Lee and W. Jeong, *Free Radical Biology and Medicine*, , DOI:10.1016/j.freeradbiomed.2015.12.023.
18 T. J. Jönsson, L. C. Johnson and W. T. Lowther, *Nature*, 2008, **451**, 98–101.
19 T. E. Forshaw, J. A. Reisz, K. J. Nelson, R. Gumpena, J. R. Lawson, T. J. Jönsson, H. Wu, J. E. Clodfelter, L. C. Johnson, C. M. Furdui and W. T. Lowther, *Antioxidants*, 2021, **10**, 946.

20 Y. F. Dufrêne, T. Ando, R. Garcia, D. Alsteens, D. Martinez-Martin, A. Engel, C. Gerber and D. J. Müller, *Nature Nanotechnology*, 2017, **12**, 295–307.

21 I. Munguira, I. Casuso, H. Takahashi, F. Rico, A. Miyagi, M. Chami and S. Scheuring, *ACS Nano*, 2016, **10**, 2584–2590.

22 P. E. Milhiet, V. Vié, M.-C. Giocondi and C. L. Grimellec, *Single Molecules*, 2001, **2**, 109–112.

23 D. A. Heesterbeek, B. W. Bardoel, E. S. Parsons, I. Bennett, M. Ruyken, D. J. Doorduijn, R. D. Gorham Jr, E. T. Berends, A. L. Pyne, B. W. Hoogenboom and S. H. Rooijakkers, *The EMBO Journal*, 2019, **38**, e99852.

24 J. Strasser, R. N. de Jong, F. J. Beurskens, G. Wang, A. J. R. Heck, J. Schuurman, P. W. H. I. Parren, P. Hinterdorfer and J. Preiner, *Nano Lett.*, 2019, **19**, 4787–4796.

25 B. Knoops, S. Becker, M. A. Poncin, J. Glibert, S. Derclaye, A. Clippe and D. Alsteens, *Cell Chemical Biology*, 2018, **25**, 550-559.e3.

26 H. Clausen-Schaumann, M. Seitz, R. Krautbauer and H. E. Gaub, *Current Opinion in Chemical Biology*, 2000, **4**, 524–530.

27 M. L. Hughes and L. Dougan, *Rep. Prog. Phys.*, 2016, **79**, 076601.

28 M. Gaczynska and P. A. Osmulski, *Current Opinion in Colloid & Interface Science*, 2008, **13**, 351–367.

29 T. Haruyama, T. Uchihashi, Y. Yamada, N. Kodera, T. Ando and H. Konno, *Journal of Molecular Biology*, 2018, **430**, 602–610.

30 R. Charoenwattanasatien, H. Tanaka, K. Zinzius, A. K. Hochmal, R. Mutoh, D. Yamamoto, M. Hippler and G. Kurisu, *Acta Crystallographica Section F Structural Biology Communications*, 2018, **74**, 86–91.

31 M. A. B. Morais, P. O. Giuseppe, T. A. C. B. Souza, T. G. P. Alegria, M. A. Oliveira, L. E. S. Netto and M. T. Murakami, *Journal of Biological Chemistry*, 2015, **290**, 8582–8590.

32 C. A. Tairum, M. C. Santos, C. A. Breyer, R. R. Geyer, C. J. Nieves, S. Portillo-Ledesma, G. Ferrer-Sueta, J. C. Toledo, M. H. Toyama, O. Augusto, L. E. S. Netto and M. A. de Oliveira, *Scientific Reports*, 2016, **6**, 33133.

33 S. Barranco-Medina, S. Kakorin, J. J. Lázaro and K.-J. Dietz, *Biochemistry*, 2008, **47**, 7196–7204.

34 K. J. Nelson, A. Perkins, A. E. D. Van Swearingen, S. Hartman, A. E. Brereton, D. Parsonage, F. R. Salsbury, P. A. Karplus and L. B. Poole, *Antioxidants & Redox Signaling*, 2018, **28**, 521–536.

35 N. A. Yewdall, T. M. Allison, F. G. Pearce, C. V. Robinson and J. A. Gerrard, *Chem. Sci.*, 2018, **9**, 6099–6106.

36 X. Roussel, G. Béchade, A. Kriznik, A. Van Dorsselaer, S. Sanglier-Cianferani, G. Branlant and S. Rahuel-Clermont, *J. Biol. Chem.*, 2008, **283**, 22371–22382.

37 T. J. Jönsson, A. W. Tsang, W. T. Lowther and C. M. Furdui, *J. Biol. Chem.*, 2008, **283**, 22890–22894.

38 C. A. Tairum Jr., M. A. de Oliveira, B. B. Horta, F. J. Zara and L. E. S. Netto, *Journal of Molecular Biology*, 2012, **424**, 28–41.

39 K. H. Koo, S. Lee, S. Y. Jeong, E. T. Kim, H. J. Kim, K. Kim, K. Song and H. Z. Chae, *Archives of Biochemistry and Biophysics*, 2002, **397**, 312–318.

40 M. Jara, A. P. Vivancos and E. Hidalgo, *Genes to Cells*, 2008, **13**, 171–179.

41 L. M. Randall, J. Dalla Rizza, D. Parsonage, J. Santos, R. A. Mehl, W. T. Lowther, L. B. Poole and A. Denicola, *Free Radical Biology and Medicine*, 2019, **141**, 492–501.

42 A. Bersweiler, B. D'Autréaux, H. Mazon, A. Kriznik, G. Belli, A. Delaunay-Moisan, M. B. Toledano and S. Rahuel-Clermont, *Nature Chemical Biology*, 2017, **13**, 909–915.

43 L. Wildling, B. Unterauer, R. Zhu, A. Rupprecht, T. Haselgrübler, C. Rankl, A. Ebner, D. Vater, P. Pollheimer, E. E. Pohl, P. Hinterdorfer and H. J. Gruber, *Bioconjugate Chem.*, 2011, **22**, 1239–1248.

44 A. Ebner, L. Wildling, A. S. M. Kamruzzahan, C. Rankl, J. Wruss, C. D. Hahn, M. Hölzl, R. Zhu, F. Kienberger, D. Blaas, P. Hinterdorfer and H. J. Gruber, *Bioconjugate Chem.*, 2007, **18**, 1176–1184.

45 M. Rief, M. Gautel, F. Oesterhelt, J. M. Fernandez and H. E. Gaub, *Science*, 1997, **276**, 1109–1112.

46 M. S. Z. Kellermayer, L. Grama, Á. Karsai, A. Nagy, A. Kahn, Z. L. Datki and B. Penke, *J. Biol. Chem.*, 2005, **280**, 8464–8470.

47 D. Alsteens, C. B. Ramsook, P. N. Lipke and Y. F. Dufrêne, *ACS Nano*, 2012, **6**, 7703–7711.

48 F. Gräter, J. Shen, H. Jiang, M. Gautel and H. Grubmüller, *Biophysical Journal*, 2005, **88**, 790–804.

49 X. Roussel, A. Kriznik, C. Richard, S. Rahuel-Clermont and G. Branlant, *J. Biol. Chem.*, 2009, **284**, 33048–33055.

50 M. Grandbois, *Science*, 1999, **283**, 1727–1730.

51 S. Garcia-Manyes and A. E. M. Beedle, *Nature Reviews Chemistry*, 2017, **1**, 1–16.

52 I. Popa, R. Berkovich, J. Alegre-Cebollada, C. L. Badilla, J. A. Rivas-Pardo, Y. Taniguchi, M. Kawakami and J. M. Fernandez, *J. Am. Chem. Soc.*, 2013, **135**, 12762–12771.

53 J. Alegre-Cebollada, R. Perez-Jimenez, P. Kosuri and J. M. Fernandez, *J. Biol. Chem.*, 2010, **285**, 18961–18966.

54 T. B. Kahn, J. M. Fernández and R. Perez-Jimenez, *Journal of Biological Chemistry*, 2015, **290**, 14518–14527.

55 J. Liang and J. M. Fernández, *ACS Nano*, 2009, **3**, 1628–1645.

56 H. A. Woo, S. W. Kang, H. K. Kim, K.-S. Yang, H. Z. Chae and S. G. Rhee, *J. Biol. Chem.*, 2003, **278**, 47361–47364.

57 B. Biteau, J. Labarre and M. B. Toledano, *Nature*, 2003, **425**, 980–984.

58 S. Ghaemmaghami, W.-K. Huh, K. Bower, R. W. Howson, A. Belle, N. Dephoure, E. K. O'Shea and J. S. Weissman, *Nature*, 2003, **425**, 737–741.

59 S. Akter, L. Fu, Y. Jung, M. L. Conte, J. R. Lawson, W. T. Lowther, R. Sun, K. Liu, J. Yang and K. S. Carroll, *Nature Chemical Biology*, 2018, **14**, 995–1004.

60 S. Stöcker, M. Maurer, T. Ruppert and T. P. Dick, *Nat Chem Biol*, 2018, **14**, 148–155.